PCCP

Physical Chemistry Chemical Physics

Accepted Manuscript

PCCP

Physical Chemistry Chemical Physics

rsc.li/pccp

Volume 19
Number 1
7 January 2017
Pages 1-896

ISSN 1463-9076

PAPER
H.-P. Loock et al.
Determination of the thermal, oxidative and photochemical
degradation rates of scintillator liquid by fluorescence EEM
spectroscopy.

ROYAL SOCIETY
OF CHEMISTRY

This is an Accepted Manuscript, which has been through the Royal Society of Chemistry peer review process and has been accepted for publication.

Accepted Manuscripts are published online shortly after acceptance, before technical editing, formatting and proof reading. Using this free service, authors can make their results available to the community, in citable form, before we publish the edited article. We will replace this Accepted Manuscript with the edited and formatted Advance Article as soon as it is available.

You can find more information about Accepted Manuscripts in the Information for Authors.

Please note that technical editing may introduce minor changes to the text and/or graphics, which may alter content. The journal's standard Terms & Conditions and the Ethical guidelines still apply. In no event shall the Royal Society of Chemistry be held responsible for any errors or omissions in this Accepted Manuscript or any consequences arising from the use of any information it contains.

ROYAL SOCIETY
OF CHEMISTRY

rsc.li/pccp

ARTICLE

Improved lifetime and stability of copper species in hierarchical, copper-incorporated CuSAPO-34 verified by catalytic model reactions

Guro Sørli,[a§] Muhammad Mohsin Azim [a‡], Magnus Rønning[b±] , and Karina Mathisen [*a†]

The first successful synthesis of hierarchical CuSAPO-34 (3.9 wt.% Cu) is reported using the polymer Pluronic F127 as mesoporous structure directing agent (SDA). X-ray absorption spectroscopy (XAS) proved single site Cu^{2+} with 4 nearest oxygen neighbours at 1.95 Å. The catalytic model reaction, selective reduction of NO with different sized hydrocarbons as reductant, explained that Cu^{2+} is accessible and reactive in both micro- and mesopores of the hierarchical CuSAPO-34. The presence of mesopores resulted in superior lifetime for the hierarchical CuSAPO-34 in the catalytic model reaction selective oxidation of propene.

1. Introduction

Copper-containing SAPO-34 is active towards methane activation [1,2] and reduction of nitrogen oxides (NO_x), [3-5] where copper is typically introduced by post modification such as ion exchange. However, this method often leads to copper species prone to migration during hydrothermal treatments, resulting in inactive CuO_x species.[1,6,7] The ion exchanged Cu:SAPO-34 is also found to deactivate due to structural degradation and formation of copper-aluminate like species promoted by hydrolysis.[3] Thus, modifying copper introduction to increase copper stability and ensuring copper specie homogeneity is of special interest. This can be done by incorporating Cu^{2+} into the SAPO-34 framework through isomorphous substitution. However, this is challenging due to many factors; one being that Cu^{2+} prefers a distorted octahedral coordination which interferes with the tetrahedral sites in the three-dimensional SAPO-34. Secondly, it is well known that during hydrothermal synthesis at temperatures above 190°C, Cu^{2+} autoreduces to Cu^+ which subsequently disproportionates to Cu^0 and Cu^{2+}.[8] Lastly, the amines used as structure directing agents (SDAs) for the synthesis of zeotypic framework may complex with Cu^{2+} making it difficult to incorporate the metal into the framework.[9,10] Therefore, the number of studies performed on CuSAPO-34 where Cu^{2+} is incorporated by isomorphous substitution are scarce.[11]

Furthermore, SAPO-34 being a small-pore zeotype, is prone to diffusion limitations especially in catalytic reactions including hydrocarbons due to coke build-up.[12-15] These issues can be

solved by strategic modification of porosity to obtain a hierarchical porous material, hence a zeotype with both micro- and mesopores. This is found to significantly enhance the lifetime of the catalyst when compared to the conventional, microporous analogue.[16-18] Metal-free hierarchical SAPO-34 has previously been reported by a co-templating strategy, where in addition to the microporous SDA (microSDA) such as tetraethylammonium hydroxide (TEAOH), organosilanes such as dimethyloctadecyl[3-trimethoxysilyl)propyl]ammonium chloride (TPOAC) or polymers such as polyethylene glycol (PEG) 2000 are added as mesoporous SDA (mesoSDA).[17,19] However, to the authors knowledge, the controlled functionalization of hierarchical CuSAPO-34 where copper is isomorphously substituted during a one-pot synthesis has not been previously reported.

Therefore, the aim of this study is the incorporation of copper through isomorphous substitution into hierarchical SAPO-34, creating single-site copper. Hence, designing a material with enhanced diffusion and lifetime compared to the conventional copper-incorporated CuSAPO-34. Further, the employment of two different catalytic model reactions will be presented to examine siting of Cu^{2+} and the porosity of hierarchical CuSAPO-34. The first is selective catalytic reduction of NO and NO_2 (designated NO_x) aided by different sized hydrocarbon reductants (HC-SCR) employed to examine the reactant selectivity of the two catalysts. An important parameter for successful synthesis of hierarchical CuSAPO-34 is being able to identify the copper siting in the material as this may affect subsequent shape selective properties and hence the catalytic abilities. The conversion of larger, bulkier reactants than what can typically fit in a micropore analogue can confirm the presence of an active site (in this case Cu^{2+}) within a mesopore.[17,20] The second reaction, selective oxidation of propene, will be exploited to compare how presence of

a. Department of Chemistry, NTNU, 7491 Trondheim
b. Department of Chemical Engineering, NTNU, 7491 Trondheim

mesopores affects the lifetime of the catalyst, where extended lifetime is characteristic for hierarchical materials. [17,21]

2. Experimental

2.1. Synthesis

Prior to the synthesis of hierarchical CuSAPO-34 a selection of mesoSDAs (CTAB, CTAOH, TMOS, DMOS, DMOCl, SDBS, Glucose, Behenic acid, P123, PEO, TTAB, F127) were investigated in a preliminary study (ESI A). Three quaternary microSDAs (TEAOH, TPAOH and TMAOH) were investigated in a parameter study for the synthesis of phase pure CHA. Here, the strategy was to employ one selected mesoSDA and TEAOH as a fixed pair and then investigating the effect of TEAOH:Al ratio, P:Al ratio and co-templating TEAOH with either TPAOH or TMAOH (for experimental details see ESI A and B).

In a typical synthesis procedure copper(II) oxide(CuO, ≥99 %, VWR Chemicals, 0.278 g) was dissolved in orto-phosphoric acid (H_3PO_4, 85wt.%, Merck, 7.96 g) and mixed with water (12.3 g) in a beaker. A suspension of pseudoboehemite (AlOOH, 75 wt.%, Sasol, 4.90 g) was prepared with the microSDAs tetraethylammonium hydroxide (TEAOH, 40 wt.%, Sigma-Aldrich, 23.2 g) and tetrapropylammonium hydroxide (TPAOH, 40 wt.%, Sigma-Aldrich, 7.0 g) in another beaker and stirred for 1 hour. Then, colloidal silica (SiO_2, 40 wt.%, Sigma-Adrich, 5.18 g) was added dropwise to the SDA-mixture and stirred for 30 minutes. Thereafter, the contents of the two beakers were mixed and aged for 2 hours. Lastly, the mesoSDA Plurionic® F-127 (~12,600 g/mol, Sigma-Aldrich, 0.5 g) dissolved in water (5 g) was added and aged for 30 minutes giving a molar ratio of 1 Al : 1 P : 0.5 Si : 0.05 Cu: 0.8 TEAOH : 0.2 TPAOH : 0.0004 F127 : 30 H2O. The gel was transferred to a 50-ml Teflon-lined stainless-steel autoclave and heated in an oven at 150°C for 120 hours. After cooling the sample was washed with deionized water and centrifuged until a clear wash water was obtained. Calcination was done in static air at 550°C for 6 hours using a heating rate of 1°C/min. For comparison, a conventional CuSAPO-34 was synthesized employing the following theoretical molar ratio: 1 Al : 1.2 P : 0.5 Si : 0.05 Cu : 1 TEAOH : 30 H_2O. The procedure was similar as above, albeit crystallized for 144 hours at 150°C.

2.2. Material characterization

Powder X-ray diffractograms were recorded on a Bruker D8 A25 DaVinci diffractometer with Cu K_α radiation in combination with a LynxEye™ SuperSpeed 1D detector. The diffractograms were recorded covering the angular interval of 5-60° (2θ) with a step size of 0.013° using a constant slit opening of 0.1 mm. For surface area, pore volume and pore diameter, a micromeritics Tri Star 3000 Surface Area and Porosity Analyzer was used. Samples were weighed out (20-40 mg) and set to degas at 250°C for 16 hours prior to analysis. Filler rods were used to minimise measuring errors. The specific surface area is calculated according to BET (Brunauer-Emmett-Teller) method, and the pore size distribution and pore volumes were calculated according to the BJH (Barrett-Joyner-Halenda) method

employing the desorption isotherm. The t-plot method was used to determine the micropore area and the external surface area of the zeotypes.

The elemental analyses were performed on a High Resolution Inductively Coupled Plasma ELEMENT 2 connected to a mass spectrometer. Samples were prepared by weighing them (10-20 mg) in a Teflon tube (25 mL) and decomposed using nitric acid (HNO_3, 65 wt.%, 1.5 mL) and hydrofluoric acid (HF, 40 wt.%, 0.5 g). The samples were then transferred to a 250 mL Teflon container and diluted using Milli-Q water until a final concentration of HNO_3 was 0.1 M. A Teflon tube (16 mL) was then washed with Milli-Q water before it was subsequently filled with the sample solution. Lastly, three blanks were prepared to eliminate background noise.

Scanning electron microscopy (SEM) was done using a Hitachi S-3400N where samples were mounted on a sample holder using carbon tape and coated with gold for 1 minute and 20 seconds using low-vacuum sputtering. The SE detector was used and a voltage of 5 eV was applied. SEM images were taken at low magnification (700 eV), medium magnification (1.6 keV) and high magnification (4.5 keV). The average particle size was determined using the software ImageJ where the image calibrated by size to obtain the correct pixel size.[22] Band-pass filter was applied to even the illumination before the image was subjected to correct threshold. For agglomerated crystals the outlines of the crystals were marked before particles analysed and the reported area was converted to size under the approximation of square particles.

CO adsorption using FTIR analysis was performed by pressing samples into a pellet (~15 mg). The pellet was subsequently transferred to the vacuum cell coupled to vacuum pumps and the FTIR (Bruker Vertex 80). The sample was dehydrated under vacuum using a heating rate of 5°C/min and held at 500°C for one hour. The sample was cooled to room temperature and subsequently, the cell was cooled to liquid nitrogen temperature (-196°C) and CO was introduced onto the sample until reaching a pressure of approximately 8 mbar. Thereafter, CO was removed stepwise using a difference of 0.05 mbar of CO for each step until no more change in OH- or CO-region was observed with a final pressure around 0.0009 mbar. The spectra obtained were normalized by weight, and the area underneath the peaks in the OH-region was integrated by means of Origin Pro 8, where the baseline was created, and peaks were found by the method of local maximum before the peaks were integrated.

2.3. X-ray absorption collection and data analysis

X-ray absorption data collection was performed at the Swiss-Norwegian Beam Lines (SNBL) at BM31 at the European Synchrotron Radiation Facility (ESRF), using a hybrid filling mode giving a maximum current of 200 mA. The beam line is equipped with a bending magnet that collects the white beam from the storage ring and a Si(111) double crystal monochromator for EXAFS data collection. Both the incident (I_0) and transmitted ($I_1 + I_2$) intensities were detected with ion chambers filled with pure N_2 at 1.3 bar (I_0) and 55% N_2 and 45% Ar ($I_1 + I_2$) at the

copper K-edge. Samples and references (CuO, Cu$_2$O, Cu(OH)$_2$ and Cu^{2+} tutton) were placed in aluminium sample holders, mixed together with boron nitride for optimal absorption and taped in place using Kapton® tape. The copper XAS data was collected using transmission mode in the scan range of 8900 – 9600 eV with a step size of 0.5 eV and counting time of 300 ms. XAS data collection was also performed at the Balder beam line at MAX IV using a multibunch filling mode reaching a maximum current of 250 mA. The beam line is equipped with an in-vacuum wiggler collecting the white beam from the storage ring, and a Si(111) double crystal monochromator for EXAFS collection. The incident (I$_0$) and the transmitted (I$_1$ + I$_2$) intensities were detected with ion chambers filled with N$_2$ (0.9 bar) and He (0.6 bar) for I$_0$, and Ar (0.2 bar) and N$_2$ (1.8 bar) for I$_1$ and I$_2$. Samples and references were measured using fly scan mode from 8729 – 9879 eV with a total number of 4095 points using a counting time of 30 ms for each point.

The Athena software from the IFFEFITT package [23] was used for data reduction where the collected data was binned (edge region -30 to 50 eV; pre-edge grid 10 eV; XANES grid 0.5 eV; EXAFS grid 0.05 Å^{-1}) and normalized before it was energy corrected in accordance to the copper foil (E$_0$ = 8979 eV). X-ray absorption near edge spectroscopy (XANES) spectra were normalized from 30-150 eV above the edge, and the copper k-edge absorption energy (E$_0$) was defined as halfway up the edge for all unknown samples. Extended X-ray absorption fine structure (EXAFS) data was normalized from 150 eV above the edge until the end of the scan, and data was deglitched and/or truncated attentively at the end of the EXAFS spectra if needed. The background was checked and corrected to obtain overlap with the total absorption μ(E) using the Autobk algorithm for background determination and normalization. The EXAFS least-square refinements were carried out using DL-EXCURV [24], where the theoretical χ$_i^{th}$(k) is fitted to the experimental χ$_i^{exp}$(k) using the curved wave theory. Ab initio phase shifts were calculated and verified when fitting references.

The nearest absorber-backscatter pair was refined by refining the energy correction factor (EF), multiplicity, Debye-Waller factor (2σ^2), and bond distance while keeping the amplitude reduction factor (AFAC) = 1. Multiplicities and bond distances must represent true, comparable values from literature and model compounds. The Debye-Waller factor must lie within 0.007 – 0.03 for acceptance of fit in samples. Thereafter, the secondary absorber-backscatter was examined by the same procedure. In particular, the direct Cu-Cu interaction (originating from metallic Cu^0) and the secondary Cu-O-Cu interaction (CuO$_x$) was thoroughly examined. Potential presence of these confirms existence of copper particles (copper phase) which oppose incorporation by isomorphous substitution. To verify the type of backscattering atoms in the second shell, Fourier filtering was used to extract the contribution in-between 2.6 to 3.2 Å in R-space. The contribution was transformed back to k-space and refined with following contributions: Cu…Cu, Cu…T, Cu…O.

The AFAC is correlated with the multiplicity and the Debye-Waller factor. AFAC was therefore extracted from CuO [25] and Cu$_2$O [25], and decorrelated from the Debye-Waller factor using both k- and k^3-weighting. The respective AFAC from CuO$_x$ were used for

refinements where contribution of Cu-O-Cu was confirmed. AFAC for as prepared and calcined samples were decorrelated by fixing the energy correction factor, multiplicity and bond distances while stepwise changing AFAC and refining the corresponding Debye-Waller factor using k^2 and k^3 weighting scheme.[26] A k^3-weighting was used for all samples, with a typical k-range of 2 – 12 Å^{-1}. The stability of the fit was tested by alternating the k-weighting between k^3 to k accepting the best fit for both weighting schemes. The goodness of fit for each refinement is given by the statistical R-factor which is defined by equation (1) and the fit index (FI) in equation (2).

$$R = \sum_i^N \left[\frac{1}{\sigma_i} (|\chi_i^{exp}(k) - \chi_i^{th}(k)|] \right) \times 100\% \qquad (1)$$

$$FI = \sum_i \frac{1}{\sigma_i} \left[\chi_i^{exp}(k) - \chi_i^{th}(k) \right]^2 \qquad (2)$$

Linear combination fitting (LCF) was performed in Athena on the respective XANES and chi-curves on spent samples, where the normalized XANES were fitted using a range starting 20 eV below the absorption edge to 30 eV above the edge. The model compounds used were: Cu$_2$O, CuO and the fresh, calcined XANES of the respective sample representing single site Cu^{2+}. The chi-curves were fitted in the k-space of 2-12.

2.4. Catalytic model reactions

The selective reduction of NO$_x$ using different sized hydrocarbons as reductants was exploited to examine the reactant selectivity of the catalysts. Here, the samples (0.212-0.425 mm, 40 mg) were transferred to a glass-lined steel reactor and kept in place with quartz wool. Samples were heated overnight in Ar (5 ml/min) reaching a temperature of 500°C before the samples were activated in O$_2$ (2 %) for 1 hour. The reaction was set to proceed at 400°C with a gas reaction mixture of O$_2$ (2% in He), NO (1000 ppm in He) and the hydrocarbon component (1000-10000 ppm in He) giving weight hourly space velocity of 0.6 – 1 g$_{reactants}$/g$_{catalyst}$*h depending on hydrocarbon concentration and component. Propene (4.5 Å) was first employed as the hydrocarbon reductant before the sample was again activated in O$_2$ for 1 hour at 500°C. Subsequently, isobutane (5.3 Å) (1000 – 10000 ppm in He) was introduced as hydrocarbon reductant at the reaction temperature of 400°C. The exhaust was monitored similarly as for propene oxidation and the NOx conversion was calculated according to equation (3).

NO conversion (%) = 100% * ([NO$_{in}$]-[NO$_{out}$])/[NO$_{in}$]   (3)

To examine the lifetime of the catalysts selective propene oxidation using molecular oxygen was employed. Sieved sample (0.212-0.425 mm, 20 mg) was transferred to a glass-lined steel reactor and kept in place by quartz wool. The sample was heated overnight to 500°C in argon flow (5 ml/min) before activation in oxygen (2%, 20 ml/min) for 1 hour. Reaction was set to proceed at 400°C for 120 hours using a reaction mixture of propene (6000 ppm) and oxygen (12000 ppm) with a weight hourly space velocity of 1.67 g$_{reactants}$/g$_{catalyst}$*h. Subsequently, the reaction was set to proceed at 450°C where the first 70 hours and hours 82-94 were performed in dry feed. Hours 70-82 and 94-100 the gas feed was sent through a bubbler holding

ARTICLE

Journal Name

47°C introducing water vapor into the system to monitor the catalysts' ability to withstand water vapor. The exhaust feed was monitored using FTIR analyzer DX4000 from Gasmet and the propene conversion was calculated according to equation 2 above, albeit with propene. Spent samples were analysed by XAS to obtain information about the stability of incorporated copper species.

3. Results and discussion

3.1. Phase purity and porosity of hierarchical CuSAPO-34

It has been established that the incorporation of Cu^{2+} into a zeotypic framework requires microSDAs that withstands complexation and/or autoreduction of the copper cation during synthesis.[8] If the SDA interacts, the net results is formation of Cu^0 in the as prepared sample which in turn becomes nanoparticlate CuO_x after calcination.[8] The copper cation is therefore not incorporated into the framework of the zeotype, even though some cations may exist as isomorphously substituted into the framework and not as nanoparticulate Cu^0/CuO_x. Similarly, the synthesis of hierarchical CuSAPO-34 also requires the use of a mesoSDA that does not hinder incorporation of Cu^{2+}. In this study, out of 11 possible mesoSDAs, only the polymer F127 was found applicable during the initial testing of well-known mesoSDAs used for the synthesis of hierarchical zeotypes. All other were found to autoreduce or complex with the copper cation leading to precipitate formation and therefore deemed not applicable.

In the consecutive parameter study with the microSDAs (TEAOH, TPAOH and TMAOH) investigated, phase pure hierarchical CuSAPO-34 was only obtained by increasing P:Al

ratio to 1.2 when TEAOH and F127 was used as a micro-mesoSDA pair (ESI, Table S1). Furthermore, co-templating TEAOH with TPAOH (keeping P:Al = 1 and total microSDA:Al = 1) in the presence of F127, phase pure CuSAPO-34 was produced. Even varying the TPAOH:TEAOH ratio from 1 to 0.1 yielded phase pure CuSAPO-34 proving the flexibility of the synthesis when both microSDAs are present. However, co-templating TEAOH with TMAOH yielded sodalite (SOD) phase. The selected hierarchical CuSAPO-34 (ESI, Table S1, number 17) will from hereon be referred to as H-CuSAPO-34. A conventional CuSAPO-34 (without F127 and only TEAOH as microSDA) was synthesised for comparison and will hereon be referred to as CuSAPO-34.

The hierarchical H-CuSAPO-34 and the conventional CuSAPO-34 were found to be phase pure CHA prior to (ESI, Fig. S1) and after calcination (Fig. 1). Any copper phase (Cu^0, Cu_2O, CuO) was excluded as these can typically form during synthesis if copper is hindered from being incorporated (Fig. S1). Calcination causes a slight decrease in intensity (21% and 29% for H-CuSAPO-34 and CuSAPO-34, respectively) when comparing the [1 0 0]-reflection at 9.4° (2θ) for both samples. CuSAPO-34 is found to be less crystalline than H-CuSAPO-34 and after calcination it is 57% as crystalline as the hierarchical analogue based on the intensity of the [1 0 0]-reflection.

The hierarchical and conventional CuSAPO-34 samples are blue prior to calcination and olive green after calcination, which correlates with literature for distorted octahedral copper incorporated CuAlPO-5.[27] The copper loading of H-CuSAPO-34 is found to be 3.9 wt.% which is slightly higher than that of the conventional analogue (2.8 wt.%) despite equal copper content in the initial synthesis gel (Table 1). This suggests that presence of the mesoSDA F127 may aid the copper loading for the incorporation of copper into the SAPO-34 framework.
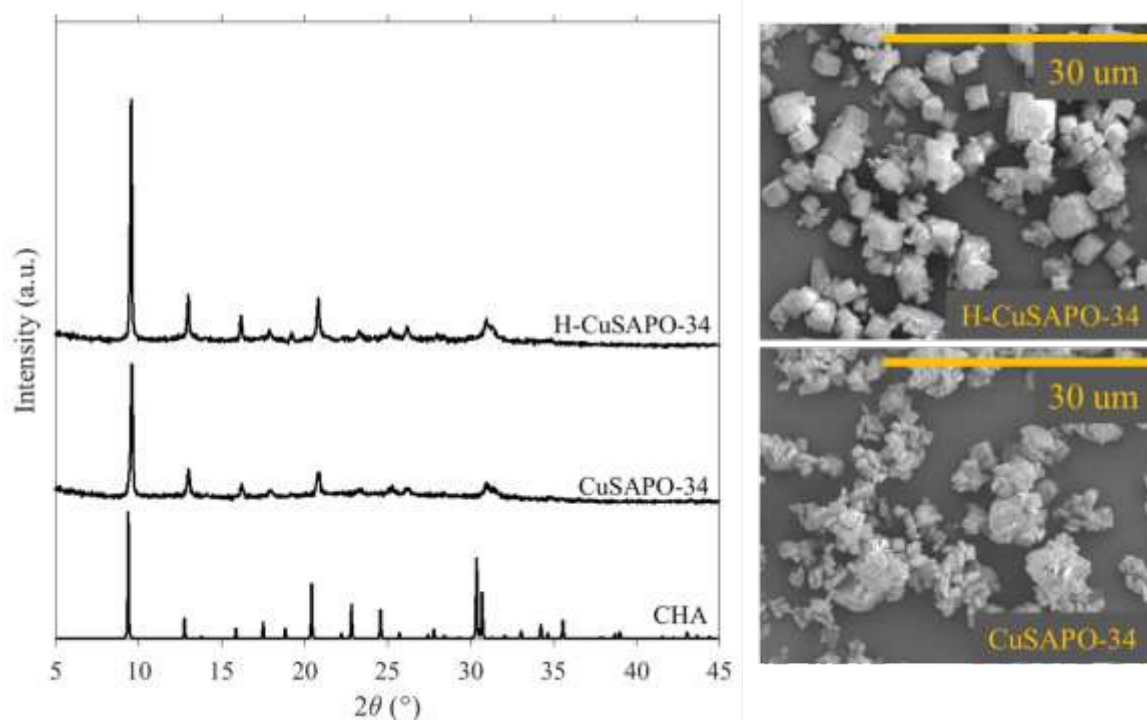

Fig. 1 XRD (left) of the calcined H-CuSAPO-34 and CuSAPO-34 showing phase purity and SEM of samples (right)

Journal Name   **ARTICLE**

The Brønsted acid strength of H-CuSAPO-34 was determined to be 276 cm^{-1} which is comparable to CuSAPO-34 (286 cm^{-1}) and literature values for SAPO-34 (around 270 cm^{-1}) (Table 1).[28,29] Isomorphous substitution of divalent transition metals is expected to form a Brønsted acid site (BAS) when an isolated Al^{3+} is replaced in the zeotypic framework. [30,31] These have been found as broad hydroxyl bands arising in the region of 3650 – 3400 cm^{-1} in metal incorporated (Me = Ti, Zr, Co, Mg, Zn) AlPOs and SAPOs.[32,33] However, due to the lack of studies in literature on the isomorphous substitution of Cu^{2+} into CHA, the exact position of such a band in CuSAPO-34 is unknown but expected to lie in the same region. In this study, evidence of such bands were not detected possibly due to the samples being subjected to vacuum prior to analysis, in which copper tends to undergo self-reduction as already established in literature. [34]

The density of acid sites was quite different as H-CuSAPO-34 contained 26 times the number of BAS in comparison to CuSAPO-34 (ESI, Fig S2). This may partially correlate to the silicon content determined by ICP-MS, where H-CuSAPO-34 is found to have (Al+P)/Si ratio equal to 13 as opposed to 25 for CuSAPO-34 (ESI, Table S2). Furthermore, H-CuSAPO-34 contains 1.5 times weak acid sites (surface groups) when compared to the conventional analogue.

H-CuSAPO-34 is found to have cubic shaped crystals (Fig. 1) with an average crystal size of 1.8 μm (Table 1) whereas the conventional analogue consists of agglomerated rectangular crystals with an average crystal size of 1 μm. In literature, the crystal size of copper-containing SAPO-34 is reported to be 1-13 μm concluding that the copper-incorporated CuSAPO-34 samples in this study lies in the lower region in comparison.[11,35] The total surface area of H-CuSAPO-34 is found to be 335 m^2/g which is slightly higher than the conventional analogue (290 m^2/g), see ESI Table S2 for results related to t-plot and pore volume. The specific surface areas are somewhat lower than that reported for plain SAPO-34. However, this is in accordance to the literature for metal incorporated SAPO-34 where it has been reported that the incorporation of metal cations decreases surface area compared to SAPO-34.[36-38] Both samples show an H4-hysteresis (Fig. S3) related to agglomerated crystals[39] or hierarchical SAPO-34[17,37,40] and no specific difference in the pore size distribution can be extracted for H-CuSAPO-34 when compared to the conventional analogue. Hence, the presence of mesopores in H-CuSAPO-34 is inconclusive based on only N$_2$ adsorption.

Table 1 Overview of physical properties such as BET surface area (N$_2$ adsorption), copper content (ICP-MS), acid strength (OH-shift from FTIR) and the average particle size derived from SEM analysis.

Sample	Surface area (m^2/g)	Cu content (wt.%)	OH-shift	Average crystal size (um)
CuSAPO-34	292	2.8	286	1
H-CuSAPO-34	335	3.9	276	1.8

3.2. Local environment of Cu^{2+}

The local copper environment was determined by X-ray Absorption Near Edge Spectroscopy (XANES, Fig. 2). Here, any formation of Cu^0 and CuO$_x$ were precluded in both the as prepared and calcined analogues independently on the porosity of the sample by comparison of the characteristic features of model compounds (Fig. S4, Fig. S5 and Fig. S6). The absorption edge energies (8986 eV) prior to calcination and the small pre-edge feature at 8977 eV for both the hierarchical and conventional CuSAPO-34 confirms that the copper species are Cu^{2+} in centrosymmetric environment such as tetragonally distorted octahedral.[27,41]

For Cu^{2+} to be successfully incorporated into the framework, the definition used in this study is that any presence of copper in the first or secondary neighbouring shell must be excluded in both as prepared and calcined CuSAPO-34. Specifically, Cu^{2+} can be deemed successfully incorporated as single site if the presence of metallic Cu-Cu distance of 2.55 Å or any oxide Cu-O-Cu distance of 2.96 Å (CuO) or 3.03 Å (Cu$_2$O) can be excluded from Extended X-ray Absorption Fine Structure (EXAFS) refinements.

Table 2 EXAFS refinements of samples as prepared and calcined showing the determined Debye-Waller factors (2σ^2), coordination numbers (N) and bond distances (R). The goodness of fit is given by R-factor (%) and the fit index (FI). The energy correction factor (EF) was refined for the as prepared samples and further transferred when refining the calcined analogues. AFAC is decorrelated and retrieved for each sample given in Fig. S7.

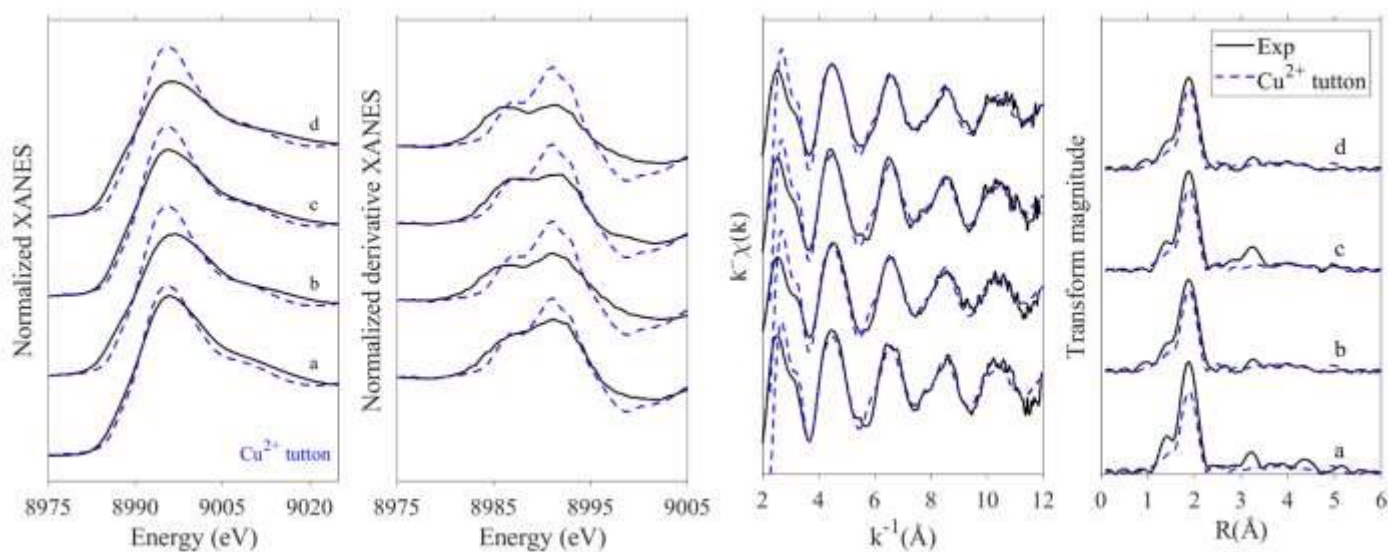| Sample	Shell	EF	2σ^2 (Å^2)	N	R (Å)	R%	FI	Δk	AFAC
CuSAPO-34 AP	Cu-O	-5.4(7)	0.010(2)	3.9(4)	1.954(7)	31.69	0.00094	2-12	0.88
	Cu…T		0.014(7)	1.3(6)	3.16(3)				
CuSAPO-34 cc	Cu-O	-5.2(6)	0.010(2)	4.0(3)	1.949(6)	29.56	0.00078	2-12	0.70
H-CuSAPO-34 AP	Cu-O	-5.5(7)	0.012(3)	3.8(4)	1.960(7)	30.70	0.00092	2-12	0.86
	Cu…T		0.008(4)	1.3(4)	3.17(2)				
H-CuSAPO-34 cc	Cu-O	-5.4(7)	0.014(3)	3.9(4)	1.957(8)	32.59	0.00100	2-12	0.79

Fig. 2 XANES (left) and EXAFS (right) of H-CuSAPO-34 (c as prepared, d calcined) and the conventional CuSAPO-34 (a as prepared, b calcined) here compared with the model compound Cu^{2+} tutton salt having tetragonally distorted Cu^{2+}.

Both H-CuSAPO-34 and CuSAPO-34 have 4 Cu-O nearest neighbours at 1.96 and 1.95 Å respectively (Table 2) for the as prepared analogues. The second shell around 3 Å can only be fitted successfully if the second backscatterer is a T-atom with a coordination number of 1-2 and a bond distance around 3.16 Å (Fig. S8). Previous studies have reported similar Cu-O…T-atom coordination numbers explained by a range of Cu-O…T-atom distances due to the tetragonal distortion of the Cu^{2+} sites.[10,27,42,43] This makes the fit more challenging as it results in low coordination numbers. Any fits including copper in the second shell results in either negative Debye-Waller factors or negative coordination number, hence no Cu-O-Cu species can be found in these samples. The contribution of a T-atom to the second shell for the as prepared analogues was further confirmed when the peak around 3 Å was Fourier Filtered showing that the shape, frequency, and amplitude of the backscattered atom has best fit with a T-atom (Fig. S9 and S10).

After calcination only the first shell at 1.96 Å (H-CuSAPO-34) and 1.95 Å (CuSAPO-34) originating from 3-4 Cu-O nearest neighbours can be found (Table 2) identical to the fresh catalysts independently of porosity, confirming the thermal stability and homogenous distribution of the copper species. Any attempt at fitting a secondary shell for the calcined samples around 3 Å was unsuccessful, indicating a larger variation in Cu…T bond distances as seen in literature.[10,27,43,44] Hence, neither metallic Cu-Cu nor Cu-O-Cu secondary neighbours can be found from EXAFS refinements.

For ion exchanged analogues the bond lengths between the copper cation and framework oxygens are typically in the range of 1.97-2.05[45,46] concluding that the bond distances found in this study are shorter (1.95 Å), indicative on a more covalent interaction with framework oxygens. The EXAFS refinements confirm that Cu^{2+} is not ejected from the CHA framework during calcination, demonstrating excellent thermal stability of the incorporated copper. No explicit copper phase is found

concluding that the copper is homogenously distributed having excellent thermal stability. A zeotypic framework is made of tetrahedrally coordinated T-atoms bridged by oxygens, which will not readily accommodate Cu^{2+} with a d^9 electronic configuration which is expected to prefer a Jahn-Teller distorted octahedral coordination.[47] Previous reports on similar CuSAPO-n indicate partial incorporation of Cu^{2+} where the copper cation is found in two different sites, one electrostatically linked to the framework and one coordinatively bonded to framework oxygens.[10,27] Therefore, Cu^{2+} can be concluded to be partially incorporated as single site into the CHA framework.

3.3. Catalytic model reactions proving hierarchy

Two catalytic model reactions are employed to provide information regarding porosity and siting of copper in the hierarchical CuSAPO-34. The first catalytic model reaction employed is selective catalytic reduction of NO which utilises Cu^{2+} to convert NO aided by a hydrocarbon reductant. In this work propene (4.5 Å) and isobutane (5.3 Å) were selected as reductants due to their varying kinetic diameter. While propene can access copper sites in both micro- and mesopores [48], isobutane [49] can only access the mesopores. The resultant NO conversions were further compared to a mesoporous Cu/ZrO₂ (6 wt.% Cu) synthesized by an evaporation-induced self-assembly (EISA) sol-gel method to exemplify NO conversion when all copper sites are found in mesopores, experimental information described elsewhere.[50]
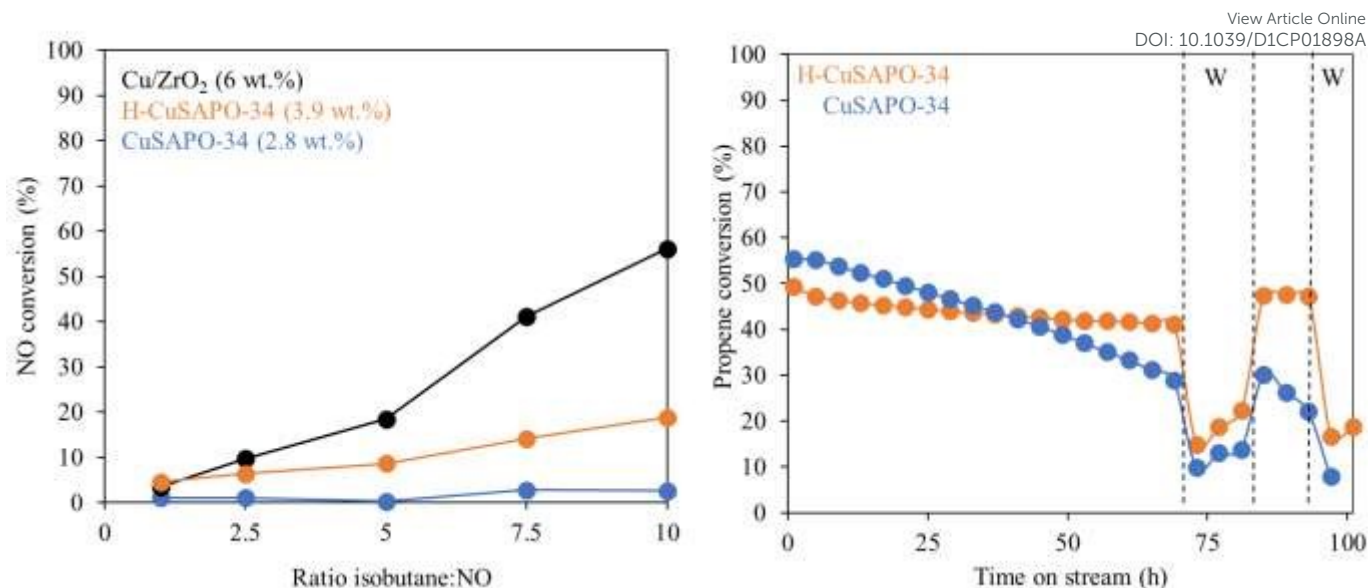
Fig. 3 Isobutane-SCR (left) showing NO conversion for H-CuSAPO-34 as opposed to CuSAPO-34 concluding presence of Cu2+ in mesopores. NO conversion for a pure mesoporous Cu/ZrO2 (black) is given for comparison. The catalytic model reaction selective oxidation of propene (right) showing extended lifetime for H-CuSAPO-34 in comparison to the conventional analogue.

The NO conversion for all three catalysts were monitored while the hydrocarbon reductant:NO ratio was varied from 1 to 10 to examine how hydrocarbon concentration affected total activity. When propene is used as a reductant hierarchical H-CuSAPO-34 show stable conversion around 30% similar to the mesoporousCu/ZrO2 for propene:NO ratio from one to five (ESI, Fig. S11). After this point the meso sized system shows a significant increase in conversion not seen for the hierarchical CuSAPO-34 which remains stable at around 30% for this whole experiment. By comparison, the NO conversion for the conventional CuSAPO-34 doubles from 14% to 28% when increasing the propene:NO ratio from 1 to 10. Conclusively, copper is accessible and reactive in the micropores of copper incorporated conventional and hierarchical CuSAPO-34 (Table 3).

When employing isobutane as hydrocarbon reductant, the deNO$_x$ activity increases linearly with increasing isobutane:NO ratio for Cu/ZrO$_2$ and H-CuSAPO-34 from 4% to 56% and 5% to 19% respectively (Fig. 3). The lower catalytic activity observed for the mesoporous Cu/ZrO$_2$ proves that propene surpasses isobutane's reduction ability. The conventional, microporous CuSAPO-34 has negligible NO conversion over the entire range. Hence, H-CuSAPO-34 must have active and accessible Cu^{2+} species in pores larger than micropores (Table 3). A remaining question is therefore how presence of the mesopores in H-CuSAPO-34 affects the catalysts' lifetime.

Hierarchical topologies have previously been reported to increase the catalysts' lifetime in several catalytic reactions due to increased diffusion as well as preventing clogging of the microporous framework.[19,21,51] In this study, selective oxidation of propene to acrolein is employed as a catalytic model reaction to monitor the catalysts' lifetime carried out at 450°C (100 hours). The active sites for this reaction are supported copper

species such as highly dispersed CuO$_x$ or copper exchanged zeolites.[52,53]

At 450°C the hierarchical CuSAPO-34 is found to have very stable propene conversion starting at 49% and declining slightly to 41% after 70 hours on stream (Fig. 3). The behaviour for CuSAPO-34 is very different, with an initial propene conversion of 55% which declines linearly to 29% concluding that the catalyst deactivates. After 37 hours on stream at 450°C, the lifetime of H-CuSAPO-34 exceeds that of the conventional concluding that presence of mesopores enhances the lifetime of the catalyst. This may suggest intraconnectivity of the micro- and mesopores in H-CuSAPO-34.

Introduction of water vapor in the reaction feed causes an overall decrease in propene conversion for both catalysts. Significantly, removal of the water vapor provides a regeneration of the active copper species in H-CuSAPO-34 as the propene conversion exceeds (47%) that the conversion prior to wet feed (41%). By contrast, the conventional CuSAPO-34 exhibits a continuous decline in propene conversion after the steam treatment. Presence of mesopores in H-CuSAPO-34 causes a superior lifetime when compared to the conventional analogue (Table 3). This may be explained by reactive and accessible Cu^{2+} in the mesopores.

The XANES of the spent CuSAPO-34 after propene oxidation reveal characteristic features of CuO (Fig 4). Formation of CuO is deemed to deactivate the catalysts as it is not an active component for acrolein formation, but rather catalyses the full oxidation of propene.[52] Presence of CuO is also seen in the chi-curve (Fig. 4, Table S4) seen by the characteristic copper shells at 2.94 Å (7 Cu) and 3.13 Å (3 Cu).[25] By contrast, the XANES of H-CuSAPO-34 show that copper is present as both Cu^{2+} and Cu$^+$ seen by the characteristic 1s-4p feature found for Cu$^+$ at 8981.6 eV (Fig. 4).
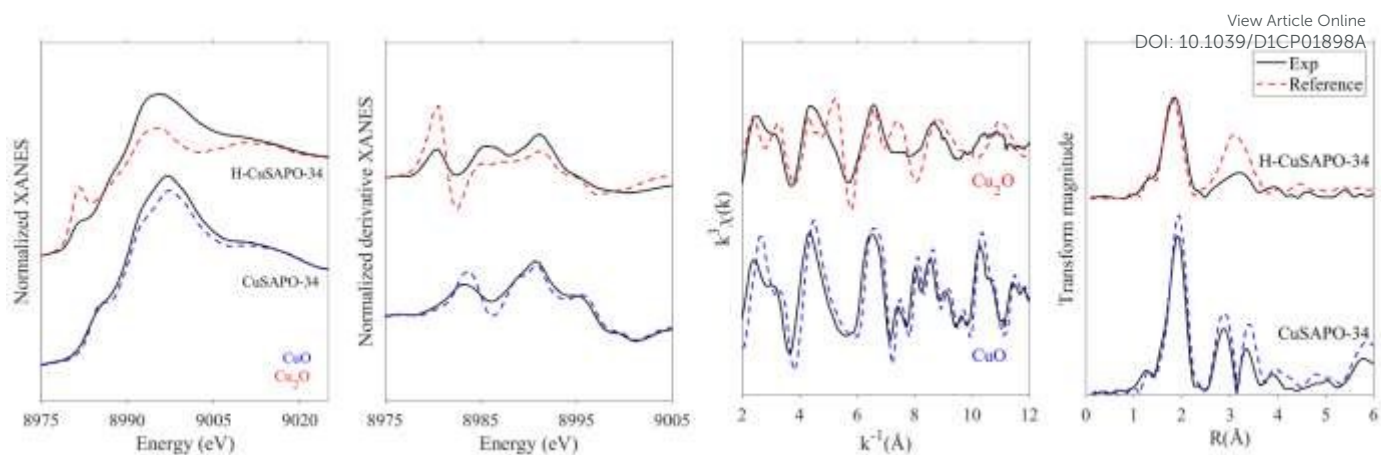
ARTICLE

Journal Name

Fig. 4 XANES (left) of the spent H–CuSAPO-34 and CuSAPO-34 after lifetime experiment with propene oxidation and the corresponding chi-curves (right) showing extensive contribution of CuO for CuSAPO-34.

Linear combination fitting (LCF, Fig. S12) was performed on the XANES and the respective chi-curves of the spent samples, showing that approximately 40% of the copper species in H-CuSAPO-34 exist as Cu^+ (XANES). The amount of CuO present in CuSAPO-34 depends if the LCF is performed on the XANES (40%) or on the chi-curve (74%), although we rely more on the LCF done on the XANES due to the respective R-factors (Fig. S11).

The EXAFS refinements show that the copper species has on average 3 nearest oxygen neighbours at 1.94 Å, very similar to the fresh catalyst (ESI, Table S2). Fitting of the second shell required Fourier filtering yielding best fit for a mixture of oxygen (2.78 Å) and copper (2.95 Å) related to small fractions of CuO. To summarise, the H-CuSAPO-34 contains less CuO compared to CuSAPO-34 concluding that the copper species in the hierarchical material are more stable for the selective oxidation of propene at harsh conditions.

Table 3 Summary of results from the catalytic model reactions employed providing information on Cu^{2+} siting and lifetime for H-CuSAPO-34 when compared to CuSAPO-34. The table is colour coded using green as yes and blue as no.

	CuSAPO-34	H-CuSAPO-34
Extended lifetime in selective propene oxidation	No	Yes
Activity Propene-SCR	Yes	Yes
Activity Isobutane-SCR	No	Yes
Cu^{2+} in micropore	Yes	Yes
Cu^{2+} in mesopore	No	Yes
Increased Cu^{2+} stability	No	Yes

Conclusions

Out of 11 possible mesoSDAs, only the polymer F127 was found to result in the first successful synthesis of copper-incorporated, hierarchical CuSAPO-34. Single site Cu^{2+} has been confirmed by X-ray absorption spectroscopy showing 4 nearest oxygen neighbours at 1.95 Å. The copper species are proven hydrothermally stable and homogenously distributed given no copper phase found from PXRD nor XAS prior and after calcination. Selective reduction of NO using different sized hydrocarbons (propene and isobutane) as reductants confirms that the hierarchical CuSAPO-34 contains copper present also in the mesosized pores. The presence of mesopores in the hierarchical CuSAPO-34 leads to superior lifetime in the catalytic model reaction selective propene oxidation. Further, XAS of the spent catalysts show that the Cu^{2+} species in the hierarchical CuSAPO-34 can withstand harsh catalytic conditions and is less prone to formation of CuO.

Author Contributions

§ Data curation, Investigation, Project administration, Validation, Visualisation, Writing – original draft

‡ Supervision, Writing- review and editing

± Project administration, Validation, Supervision, Writing – review and editing

† Conceptualization, Project administration, Resources, Supervision, Writing- review and editing

Conflicts of interest

There are no conflicts to declare.

Acknowledgements

Notes and references

1. K. P. Kvande, D.K.; Dyballa, M.; Buono, C.; Signorile, M.; Borfecchia, E.; Lomachenko, K.A.; Arstad, B.; Bordiga, S.; Berlier, G.; Olsbye, U.; Beato, P.; Svelle, S. , *Catalysts*, 2020, **10**.

2. M. J. Wulfers, S. Teketel, B. Ipek and R. F. Lobo, *Chemical Communications*, 2015, **51**, 4447-4450.

3. A. Wang, Y. Chen, E. D. Walter, N. M. Washton, D. Mei, T. Varga, Y. Wang, J. Szanyi, Y. Wang, C. H. F. Peden and F. Gao, *Nature Communications*, 2019, **10**, 1137.

4. A. M. Beale, I. Lezcano-Gonzalez, W. A. Slawinksi and D. S. Wragg, *Chemical Communications*, 2016, **52**, 6170-6173.

5. S. T. Korhonen, D. W. Fickel, R. F. Lobo, B. M. Weckhuysen and A. M. Beale, *Chemical Communications*, 2011, **47**, 800-802.

6. A. Frache, B. I. Palella, M. Cadoni, R. Pirone, H. O. Pastore and L. Marchese, *Topics in Catalysis*, 2003, **22**, 53-57.

7. F. Gao and J. Szanyi, *Applied Catalysis A: General*, 2018, **560**, 185-194.

8. A. Moen and D. G. Nicholson, *Journal of the Chemical Society, Faraday Transactions*, 1995, **91**, 3529-3535.

9. C. W. Lee, G. Brouet, X. Chen and L. Kevan, *Zeolites*, 1993, **13**, 565-571.

10. K. Mathisen, D. G. Nicholson and M. Stockenhuber, *Microporous and Mesoporous Materials*, 2005, **84**, 261-274.

11. R. Martínez-Franco, M. Moliner, C. Franch, A. Kustov and A. Corma, *Applied Catalysis B: Environmental*, 2012, **127**, 273-280.

12. D. Chen, K. Moljord and A. Holmen, *Microporous and Mesoporous Materials*, 2012, **164**, 239-250.

13. Y. Gao, S.-L. Chen, Y. Wei, Y. Wang, W. Sun, Y. Cao and P. Zeng, *Chemical Engineering Journal*, 2017, **326**, 528-539.

14. U. Olsbye, M. Bjørgen, S. Svelle, K.-P. Lillerud and S. Kolboe, *Catalysis Today*, 2005, **106**, 108-111.

15. U. Olsbye, S. Svelle, K. P. Lillerud, Z. H. Wei, Y. Y. Chen, J. F. Li, J. G. Wang and W. B. Fan, *Chemical Society Reviews*, 2015, **44**, 7155-7176.

16. Y.-R. He, Y.-L. Zhu, Y. Duan, M. Zhang and J. Jiang, *Crystal Growth & Design*, 2020, **20**, 17-23.

17. Q. Sun, N. Wang, G. Guo, X. Chen and J. Yu, *Journal of Materials Chemistry A*, 2015, **3**, 19783-19789.

18. F. Wang, L. Sun, C. Chen, Z. Chen, Z. Zhang, G. Wei and X. Jiang, *RSC Advances*, 2014, **4**, 46093-46096.

19. Q. Sun, N. Wang, D. Xi, M. Yang and J. Yu, *Chemical Communications*, 2014, **50**, 6502-6505.

20. M. Hartmann and L. Kevan, *Chemical Reviews*, 1999, **99**, 635-664.

21. G. Guo, Q. Sun, N. Wang, R. Bai and J. Yu, *Chemical Communications*, 2018, **54**, 3697-3700.

22. C. A. Schneider, W. S. Rasband and K. W. Eliceiri, *Nature Methods*, 2012, **9**, 671-675.

23. B. Ravel and M. Newville, *Physica Scripta*, 2005, DOI: 10.1238/physica.topical.115a01007, 1007.

24. S. B. G. Tomic S., Wander A., Harrison N.M., Dent A.J., Mosselmans J.F.W, Inglesfield J.E., *New Tools for the Analysis of EXAFS: The DL_EXCURV package*, Report CCLRC Technical Report DL-TR-2005-001, ISSN 1362-0207, Council for the Central Laboratory of teh Research Councils, 2005.

25. J. Ghijsen, L. H. Tjeng, J. van Elp, H. Eskes, J. Westerink, G. A. Sawatzky and M. T. Czyzyk, *Physical Review B*, 1988, **38**, 11322-11330.

26. M. Bauer and H. Bertagnolli, *The Journal of Physical Chemistry B*, 2007, **111**, 13756-13764.

27. K. Mathisen, D. G. Nicholson, A. N. Fitch and M. Stockenhuber, *Journal of Materials Chemistry*, 2005, **15**, 204-217.

28. C. Lamberti, A. Zecchina, E. Groppo and S. Bordiga, *Chemical Society Reviews*, 2010, **39**, 4951-5001.

29. G. V. A. Martins, G. Berlier, C. Bisio, S. Coluccia, H. O. Pastore and L. Marchese, *The Journal of Physical Chemistry C*, 2008, **112**, 7193-7200.

30. J. Chen and J. M. Thomas, *Journal of the Chemical Society, Chemical Communications*, 1994, DOI: 10.1039/C39940000603, 603-604.

31. B. M. Weckhuysen, R. R. Rao, J. A. Martens and R. A. Schoonheydt, *European Journal of Inorganic Chemistry*, 1999, **1999**, 565-577.

32. J. Chen, J. M. Thomas and G. Sankar, *Journal of the Chemical Society, Faraday Transactions*, 1994, **90**, 3455-3459.

33. M. Mortén, Ł. Mentel, A. Lazzarini, I. A. Pankin, C. Lamberti, S. Bordiga, V. Crocellà, S. Svelle, K. P. Lillerud and U. Olsbye, *ChemPhysChem*, 2018, **19**, 484-495.

34. E. Borfecchia, K. A. Lomachenko, F. Giordanino, H. Falsig, P. Beato, A. V. Soldatov, S. Bordiga and C. Lamberti, *Chemical Science*, 2015, **6**, 548-563.

35. S. Huang, J. Wang, J. Wang, C. Wang, M. Shen and W. Li, *Applied Catalysis B: Environmental*, 2019, **248**, 430-440.

36. M. Sedighi, M. Ghasemi, M. Sadeqzadeh and M. Hadi, *Powder Technology*, 2016, **291**, 131-139.

37. A. Z. Varzaneh, J. Towfighi and S. Sahebdelfar, *Microporous and Mesoporous Materials*, 2016, **236**, 1-12.

38. J. Zhong, J. Han, Y. Wei, S. Xu, T. Sun, X. Guo, C. Song and Z. Liu, *Journal of Energy Chemistry*, 2019, **32**, 174-181.

39. K. K. Thommes M, Neimark AV, Olivier JP, Rodriguez-Reinoso F, Rouquerol J, et al. , *Pure and Applied Chemistry*, 2015, **87(9-10)**, 1051-1069.

40. H. Yang, Z. Liu, H. Gao and Z. Xie, *Journal of Materials Chemistry*, 2010, **20**, 3227-3231.

ARTICLE

41.   M. Sano, S. Komorita and H. Yamatera, *Inorganic Chemistry*, 1992, **31**, 459-463.

42.   T. Kristiansen, K. Mathisen, M.-A. Einarsrud, M. Bjørgen and D. G. Nicholson, *The Journal of Physical Chemistry C*, 2011, **115**, 19260-19268.

43.   D. G. Nicholson and M. H. Nilsen, *Journal of Materials Chemistry*, 2000, **10**, 1965-1971.

44.   K. Mathisen, M. Stockenhuber and D. G. Nicholson, *Physical Chemistry Chemical Physics*, 2009, **11**, 5476-5488.

45.   E. Borfecchia, K. A. Lomachenko, F. Giordanino, H. Falsig, P. Beato, A. V. Soldatov, S. Bordiga and C. Lamberti, *Chemical Science*, 2015, **6**, 548-563.

46.   K. A. Lomachenko, E. Borfecchia, C. Negri, G. Berlier, C. Lamberti, P. Beato, H. Falsig and S. Bordiga, *Journal of the American Chemical Society*, 2016, **138**, 12025-12028.

47.   M. A. Halcrow, *Chemical Society Reviews*, 2013, **42**, 1784-1795.

48.   T. D. Pham and R. F. Lobo, *Microporous and Mesoporous Materials*, 2016, **236**, 100-108.

49.   M. Gehre, Z. Guo, G. Rothenberg and S. Tanase, *ChemSusChem*, 2017, **10**, 3947-3963.

50.   O. H. Bjørkedal, S. K. Regli, R. J. G. Nuguid, P. E. Vullum, O. Kröcher, D. Ferri and M. Rønning, *Catalysis Today*, 2021.

51.   D. Ali, C. R. Zeiger, M. M. Azim, H. L. Lein and K. Mathisen, *Microporous and Mesoporous Materials*, 2020, **306**, 110364.

52.   P. A. Ignacio-de Leon, M. Ferrandon, L. M. Savereide, S. L. Nauert, J. Moncada, R. Klet, K. Chapman, M. Delferro, J. Camacho-Bunquin, C. A. Carrero, J. M. Notestein and S. Nguyen, *Catalysis Letters*, 2020, **150**, 826-836.

53.   J.-s. Yu, Kevan, Larry, *J. Phys. Chem*, 1991, **95**, 6648-6653.

54.   K. Momma and F. Izumi, *Journal of Applied Crystallography*, 2011, **44**, 1272-1276.